



Effects of Nozzle Geometry on Turbulent Characteristics and Structure of Surface Attaching Jets

Mohammad Shajid Rahman¹  · Godwin Fabiola Kwaku Tay¹ · Mark Francis Tachie¹

Received: 8 February 2019 / Accepted: 17 June 2019 / Published online: 29 June 2019
© Springer Nature B.V. 2019

Abstract

The effects of nozzle exit geometry on the characteristics of a surface attaching jet were investigated experimentally. Three different types of nozzle geometries were studied, including a circular, square and rectangular nozzle with the same exit area. The jets were discharged with an offset height of two nozzle width at a Reynolds number of 5500. A particle image velocimetry system was used to measure the flow. Instantaneous visualizations revealed that the largest enhancements in the near field mixing and entrainment occur in the minor plane of the rectangular nozzle compared to the square and circular nozzles resulting in more rapid expansion of the shear layer. This also caused a faster deflection of the jet towards the free surface, maximum velocity decay and spread rates of the rectangular jet with minor axis orientation. The jet-surface interaction was examined using surface velocity, vorticity thickness and surface turbulence intensities. It was found that the damping of the surface-normal velocity fluctuations at the free surface is more severe in the minor plane of the rectangular jet than the square and circular nozzles. The influence of the free surface was also felt in the profiles of mean velocity and Reynolds stresses. The attenuation of Reynolds shear stress due to confinement was more dramatic in the minor plane of the rectangular nozzle than the other geometries. To quantify the influence of nozzle geometry on the coherent structures in the interaction region, two-point correlations of the velocity fluctuations and swirling strength; and proper orthogonal decomposition were performed.

Keywords Nozzle geometry · Particle image velocimetry · Proper orthogonal decomposition · Surface jet · Two-point correlation · Vorticity thickness

Abbreviations

AP attachment point
FOV field of view
IA interrogation area

✉ Mohammad Shajid Rahman
rahmanms@myumanitoba.ca

¹ Department of Mechanical Engineering, University of Manitoba, Winnipeg, Manitoba R3T 5V6, Canada

PIV	particle image velocimetry
POD	proper orthogonal decomposition
RANS	Reynolds-averaged Navier–Stokes
TKE	turbulent kinetic energy

1 Introduction

Confined turbulent jets such as those issuing near a free surface (hereafter referred to as surface attaching jets) are of significant interest to diverse engineering applications. Examples include spillway jets of hydro-electric power dams, industrial effluent discharging into stagnant water, and submerged wakes produced by the propulsion of naval vehicles. Some of these applications, including effluent discharging, demand enhanced mixing performance. The free surface acts to constrain the turbulent motion in the surface-normal direction, and has a direct impact on the entrainment and mixing characteristics of the jet. From the large body of literature on the subject [1, 2], the general consensus is that the effect of a strong confinement is to suppress the velocity fluctuations normal to the free surface and to reduce the velocity decay rate in comparison to a turbulent free jet which experiences no boundary confinement effect. In the context of mixing, this implies that there is a need for more fundamental research to develop more efficient mixing-control strategies to minimize the performance degradation introduced by the jet confinement. Furthermore, due to the kinematic boundary condition imposed by the free surface, the surface attaching jet is a challenging flow both for the development and testing of turbulence models [3, 4]. This study is focused on nozzle geometry which has significant impact on the mixing characteristics of turbulent free jets [5–7]. Also, the knowledge gleaned from such studies will help to promote a better understanding of the effects of nozzle geometry on the structure and dynamics of surface attaching jets.

A schematic of a surface attaching jet in the vertical jet symmetry plane is shown in Fig. 1 with the coordinate system and nomenclature adopted in the present study. The jet is discharged from a nozzle of width, d , with an exit velocity of U_j . The center of the nozzle is located at an offset height, h from the free surface. As indicated in the figure, the origin of the Cartesian coordinate system is located at the center of the nozzle in the jet exit plane; x and y denote the streamwise and surface-normal direction respectively; U and V are the streamwise and surface-normal mean velocities respectively; u and v are the streamwise and surface-normal fluctuating velocities respectively. Upon discharge, the jet attaches to the free surface at the attachment point (AP). Downstream of the AP, the flow remains attached to the free surface, where positive streamwise mean velocity (U_s) and non-zero turbulence intensity appear due to the kinematic boundary condition of a free surface [1, 8, 9]. Contrary to a free jet, the locus of local maximum mean streamwise velocity, U_m deviates from the nozzle centreline ($y/d = 0$) towards the free surface [8, 10]. The ordinate of points on the locus of U_m is denoted by y_m . An imaginary axis (the jet centerline) passing through the loci of U_m divides the jet into two shear layers: an upper shear layer and a lower shear layer. The symbols $y_{0.5}$ and $y_{0.5}^s$ denote the half velocity widths in the lower shear layer measured relative to the locus of U_m and the free surface, respectively.

The technique of modifying the nozzle geometry has been used widely in the free jet literature as a passive mixing-control methodology to enhance mixing between the jet flow and surroundings [11, 12]. Interest in this approach grew very rapidly ever since studies on elliptic and rectangular jets [13, 14] revealed the azimuthal deformation of the jet cross-section due to

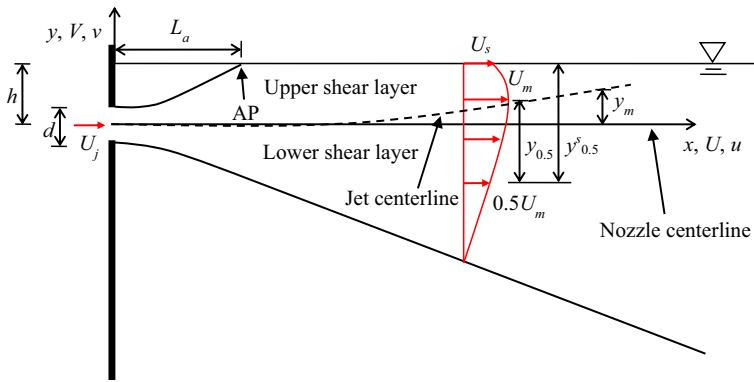


Fig. 1 A sketch of a surface attaching jet in the symmetry plane

vortex self-induction mechanism. This mechanism leads the azimuthal vortex rings to be inherently unstable, and to the axis-switching of the cross section of the jet [15]. The axis-switching phenomenon has been found to promote mixing in non-circular jets by increasing entrainment of ambient fluid when compared to circular jets. One of the earliest experiments on the effects of nozzle geometry on the evolution of turbulent free jets was conducted by Hammond [16]. In that study, free jets issuing from circular, rectangular and a four-slot nozzle were investigated. It was found that the rectangular nozzle produced a higher centerline velocity decay rate than the circular nozzle while the slot nozzle produced the highest centerline velocity decay rate in comparison to the rectangular and circular nozzles. In recent measurements using various non-circular nozzles, Aleyasin et al. [6, 7, 17] observed the production of vortical structures in the shear layers due to the Kelvin-Helmholtz instability mechanism. They identified the structures to be prograde and retrograde spanwise vortex cores in the lower and upper shear layers, respectively. They concluded that the spanwise vortices were responsible for the turbulent mixing in the jet due to their diffusion from the shear layers to the jet centreline.

For surface attaching jets, various types of nozzle geometries have been used in the past to investigate its flow features, including circular nozzles [18, 19], square nozzles [8, 20], rectangular nozzles [9] and plane nozzles [21, 22]. Most of these studies are comprehensively reviewed in Wen et al. [23, 24] and in the more recent publications by Tay et al. [8, 9]. In all of these investigations, various turbulent statistics, such as the mean velocity and Reynolds stresses, were used to characterize the interaction between the free surface and the submerged jet. Wen et al. [23, 24] applied more advanced statistical analysis tools such as the proper orthogonal decomposition (POD) method to quantify the jet-surface interaction while Tay et al. [8, 9] presented detailed two-point correlation and surface velocity measurements. However, despite its many technical applications, very little is documented on the influence of nozzle geometry on the flow dynamics of surface attaching jets. For instance, Rajaratnam and Humphries [21] reported mean streamwise velocity measurements for three surface jet configurations: a plane surface jet and two bluff (circular and rectangular) surface jets with an offset height ratio, $h/d = 0.5$. No significant differences were reported in the downstream evolution of the bluff jets but their spread and maximum mean velocity decay rates were significantly lower in comparison to the plane surface jet.

In the present work, the effects of nozzle exit geometry on the mixing characteristics and turbulence structure of a surface attaching jet were investigated. A circular, square and

rectangular nozzle were considered. In all three cases, the jet exit Reynolds number and offset height ratio were set to 5500 and 2, respectively. A high-resolution particle image velocimetry (PIV) system was used to conduct the velocity measurements. The influence of nozzle geometry on the turbulent structures was explored using instantaneous flow visualization, two-point correlations and proper orthogonal decomposition (POD).

2 Experimental Setup

The experiments were conducted in an open recirculating water channel as shown in Fig. 2a. The test section of the channel is 2500 mm long and has a cross section of dimensions 200 mm \times 200 mm. The side and bottom walls of the channel were made of clear acrylic plate that facilitates optical access. The flow in the channel was driven by a centrifugal pump through a series of flow conditioning units that include a settling chamber fitted with perforated plate, a hexagonal honey-comb and a 6.5:1 converging section. The resulting fine-scale flow then passed through the inlet section of the channel. In order to facilitate easy installation of the nozzles, a nozzle assembly consisting of a dam of 100 mm length from the channel inlet and nozzle plates was used. The dam ensures a uniform flow at the nozzle exit, and also facilitates feeding the seeding particles into the flow. The nozzle plates were made of acrylic of thickness 3 mm. The center of the nozzle was located at a distance $h = 20$ mm from

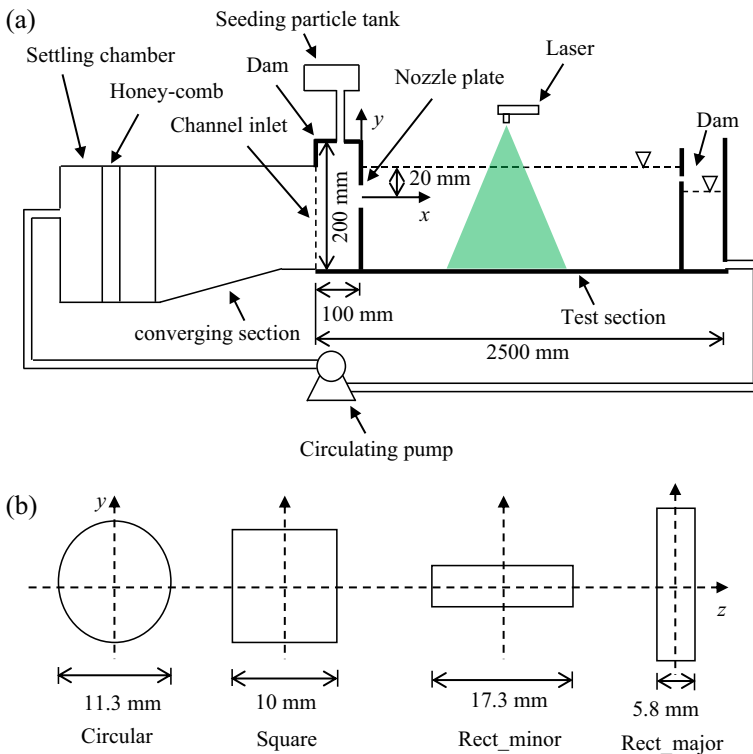


Fig. 2 Schematic diagram of (a) experimental setup and (b) nozzle geometries

the free surface to produce surface attaching jet. Another dam was used at the end portion of the test section to maintain a constant tail water depth.

The following shapes of the orifice type nozzle were tested: circular with diameter, $D = 11.3$ mm; square with a side dimension of $d = 10$ mm; and rectangular with aspect ratio of 3 (17.3 mm \times 5.8 mm) as shown in Fig. 2b. Since the rectangular nozzle is not symmetric, it was oriented with the minor (Rect_minor) and major (Rect_major) axis along the y direction. The cross-sectional area of each nozzle and the jet exit velocity, U_j were approximately 100 mm² and 0.55 m/s, respectively which ensured that the jets discharged with the same momentum flux in all cases. The offset height ratio (h/d) was maintained at 2 for each nozzle configuration. The Reynolds number, Re based on U_j and d ; and the Froude number, Fr based on U_j and h were 5500 and 1.24, respectively. The Reynolds number and Froude number were chosen based on the previous study by the authors [25] to ensure an undisturbed free surface. This is critically important to avoid distortion of the laser sheet illumination which could compromise the quality of the PIV data. For all experiments, the free surface was free of contaminants due to the clean filtered water used.

A PIV system was used to conduct detailed velocity measurement in the vertical symmetry plane of the jets. 10 μ m silver coated hollow glass spheres with specific gravity of 1.4 were used as seeding particles. The values of the estimated settling velocity (2.18×10^{-5} m/s), the response time (7.78×10^{-6} s) and Stokes number, $St \approx 0.003$ of the seeding particles ensured that the particles followed the flow closely. A Nd:YAG (neodymium-doped yttrium aluminium garnet) double-pulsed laser with maximum energy of 120 mJ per pulse at 532 nm wavelength was used to illuminate the flow field. The thickness of the laser sheet was maintained as approximately 1 mm which reduced the number of de-focused particles within the measurement plane [26]. The scattered light from the seeding particle was captured by a 12-bit charge-coupled device camera with resolution of 2048×2048 pixel and pixel pitch of 7.4 μ m. The field of view (FOV) of the camera was set to 84×84 mm², and interrogation area (IA) of 32×32 pixels with 50% overlap in both x and y directions was used to post-process the images. The time interval between pulses was set in such a way that the maximum particle displacement was smaller than 25% of the IA size. The flow field was captured in three measurement planes, covering the flow field in the streamwise direction of $0 \leq x/d \leq 24$. Based on an initial convergence test, 5000 uncorrelated image pairs were captured in each plane at 4 Hz acquisition rate. The images were post-processed by DynamicStudio which uses adaptive correlation to obtain the average particle displacement. Using the measurement uncertainty methodology proposed by Coleman and Steele [27], the uncertainties in the mean velocity, turbulence intensities and Reynolds stresses at 95% confidence level were estimated as $\pm 3\%$, $\pm 7\%$ and $\pm 10\%$, respectively of their local peak values.

3 Results and Discussion

3.1 Initial conditions

In order to assess the near-exit condition of the jets, profiles of streamwise mean velocity and streamwise turbulence intensity at $x/d = 0.5$ are examined for the different nozzle geometries in Fig. 3. The local maximum streamwise mean velocity (U_m) and individual nozzles' dimension in each plane (d_i) are used to normalize the profiles. The mean velocity profiles (Fig. 3a) depict a top-hat shape irrespective of nozzle geometries. This differs from jets issuing from a sharp-

edged orifice plate nozzle which show a characteristic saddle-backed shape, where the velocity overshoots towards the edge of the nozzle [28]. This discrepancy can be attributed to the finite thickness (≈ 3 mm) of the current nozzle plate. The relative turbulence intensity profiles (Fig. 3b) show typical low value in the central jet region since the mean velocity distributions are nearly uniform there, and peak values around the nozzle edges ($y/d_i \approx \pm 0.5$) due to presence of shear layers in that region as reported by Quinn [29], for instance. Circular, square and Rect_major jets show similar peak values of the relative turbulence intensity of about 33%. The turbulence level for the rectangular nozzle in the minor plane is 20% lower than in the major plane. The peak value of the relative turbulence intensity for the present circular and square nozzle is comparatively higher than previous studies with jet issuing from a circular orifice nozzle at Reynolds number, $Re = 16,000$ [28], a square contoured nozzle at $Re = 10,000$ [30] and a circular or square sudden contraction nozzle at $Re = 10,000$ [7]. A higher turbulence level in the present study can be attributed to different initial conditions such as nozzle type and Reynolds number, which had considerable effects on the exit turbulence level in the previous jet studies [28, 30].

3.2 Instantaneous velocity fields

The instantaneous velocity fields in the vertical symmetry planes of the non-circular jets (square, Rect_minor and Rect_major) visualized using the Galilean decomposition method are examined in Fig. 4. The circular jet is not shown here because of similarities in flow topology with the square jet. Velocity vectors within the range of streamwise distance ($0 \leq x/d \leq 7$) are shown in the plot that includes near and intermediate fields of the jets. These two regions were selected because of their significance in mixing and entrainment [31]. To reveal the instantaneous coherent structures, a constant convective velocity of $0.15U_j$ [2] was subtracted from the instantaneous streamwise velocities. Important features of the flow revealed by the Galilean-decomposition include a helical structure delineated by the longer arrows (darker areas) in the plots, braid-like structures (lighter areas) sandwiched between the helices and spanwise vortex cores (swirling motions) along the edge of the shear layers [32, 33]. The helical structure originates from the downstream propagation of the vortex rings shed by the nozzles, while the spanwise vortex cores, connected by the braids, can be attributed to the Kelvin-Helmholtz roll up of the edge of the upper and lower shear layers. To highlight the

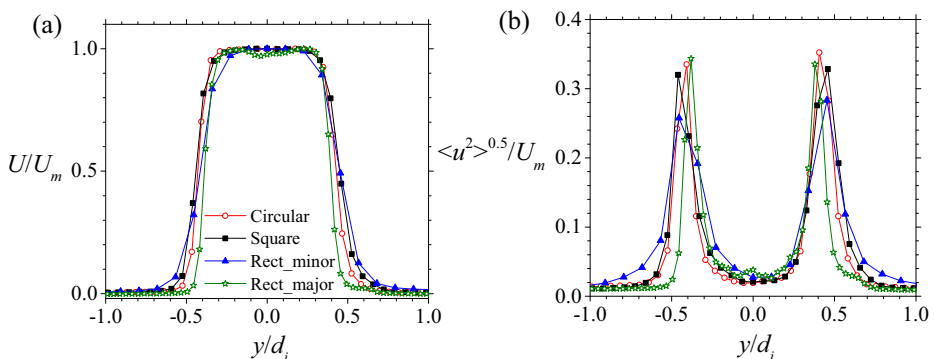
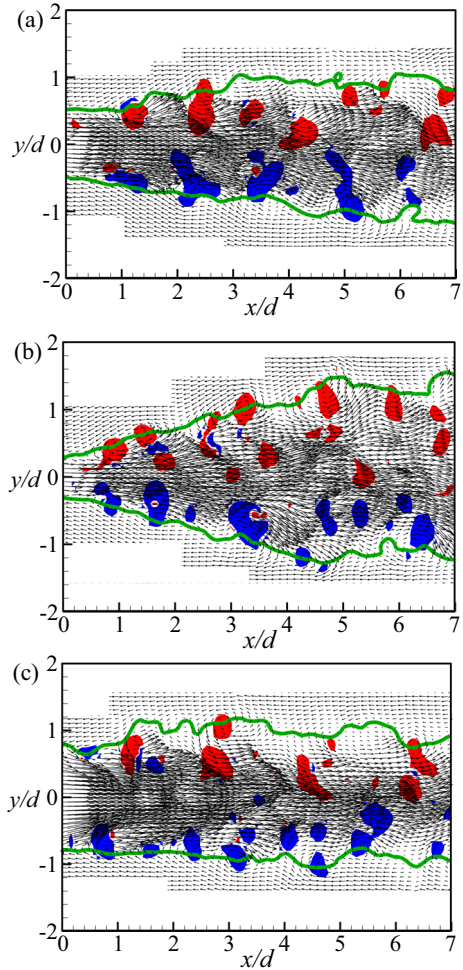


Fig. 3 Profiles of (a) streamwise mean velocity and (b) streamwise turbulence intensity at $x/d = 0.5$ for different nozzle geometries

Fig. 4 Instantaneous velocity field for (a) square, (b) Rect_minor and (c) Rect_major jet. The arrows, contours and lines indicate the velocity vectors, instantaneous swirling strength and zero-velocity contour line, respectively



direction of rotation of the spanwise vortex cores, iso-contours of instantaneous swirling strength (red and blue contours) were superimposed on the vector maps. In the plots, the red swirling strength contours correspond to counter-clockwise rotating (retrograde) vortices, while the blue contours correspond to clockwise rotating (prograde) vortices. The counter rotation of the vortices plays a major role in entraining ambient fluid into the jet. The edges of the shear layer marked by the zero-velocity contour line coincide with the centers of the vortex cores. The zero-velocity contour line also marks roughly the locus of the turbulent-nonturbulent interface where entrainment takes place [34]. As indicated by the zero-velocity contour lines in Fig. 4a (square) and Fig. 4b (Rect_minor), the width of the helical structure is ever increasing as the jet propagates downstream. This is consistent with the outward expansion of the jet as it entrains and mixes with ambient fluid. In the major plane of the rectangular nozzle (Fig. 4c), the lines are almost parallel to the free surface because of the surface-normal contraction of the jet. The latter effect is caused by the axis-switching of the major and minor planes of the jet. Qualitatively, the faster expansion of the Rect_minor jet

compared to the other nozzle geometries in the x - y plane is an indication of enhanced vertical entrainment and mixing for the Rect_minor nozzle. Similar observations of enhanced mixing and entrainment in the minor plane of a rectangular nozzle compared to round and square nozzles were reported in previous free jet investigations [7, 35].

3.3 Contours of mean velocities

Figure 5 shows the normalized mean velocity contours in the symmetry planes of the square, Rect_minor and Rect_major jets. The displayed regions span the measurement range, $0 \leq x/d < 16$, which includes the pre-attachment region and part of the interaction region. In all plots, the free surface is located at the surface-normal location $y/d \approx 2$. The effects of nozzle geometry on the streamwise mean velocity (U/U_j) are depicted in Fig. 5a, c and e. The potential core, which is significant in the near field mixing of turbulent jets, is visible in the figure. The potential core length, L_p was estimated as the length of the streamwise region beginning from the jet exit within which the maximum mean streamwise velocity remains up to approximately 98% of the jet exit velocity [7]. The values of L_p/d (Table 1) varies from approximately 3.0 for the circular nozzle (not plotted) to approximately 2.0 for the square nozzle (Fig. 5a) and Rect_minor nozzle (Fig. 5c). These results are in reasonable agreement with those reported in previous studies on free jets [5, 7, 35]. These studies reported a general decrease in the potential core length for non-circular jets compared to circular jets. The approximately 33% reduction in the value of L_p/d by the square and Rect_minor nozzles indicates higher mixing in the near field of these nozzle configurations in comparison to the circular nozzle. These results are consistent with the observations in the instantaneous visualizations. For instance, for the non-circular configurations, the enhanced mixing can be attributed to more energetic near field Kelvin-Helmholtz structures, which are more capable of entraining ambient fluid into the jet [36]. In the major plane of the rectangular nozzle (Fig. 5e) the potential core length is approximately 33% larger than the minor-axis orientation. This difference can be attributed to reduced near field mixing for Rect_major jet at the presence of a free surface causing a delay of the onset of centerline velocity decay. There is a characteristic surface-normal contraction of the Rect_major jet (mainly within $0 \leq x/d < 6$), which can be considered as an artifact of the axis-switching phenomenon. Similar observations were reported in the major planes of non-circular free jets by previous authors [6, 7, 37]. The mean streamwise velocity contour plots also show that the jets attached to the free surface after discharge from the nozzles. In each case, the attachment point (AP) was determined using the following three methods: the location where the contour of $U/U_j = 0$ attaches to the free surface, the location where the contour level of $U/U_j \approx 0.0125$ (minimum streamwise mean velocity level from the dynamic range of the PIV system) attaches to the free surface, and from the zero-crossing of the surface mean streamwise velocity profiles. The dimensionless attachment lengths (L_d/d) determined using these approaches were found to vary within a ± 0.3 margin. The values of L_d/d are summarized in the last column of Table 1. The attachment lengths of the circular and square jets are similar. This is due to their similar growth characteristics. In the case of the Rect_minor jet, the faster growth of the shear layer caused about 25% reduction in the attachment length when compared to circular and square jets. The larger attachment length in the major plane of the rectangular jet (Rect_major) should be expected because of the limited vertical growth of the shear layer in this case that supports reduced near field entrainment and mixing. This effect, which is due to the axis-switching, delays the onset of the jet-surface interaction for the Rect_major configuration.

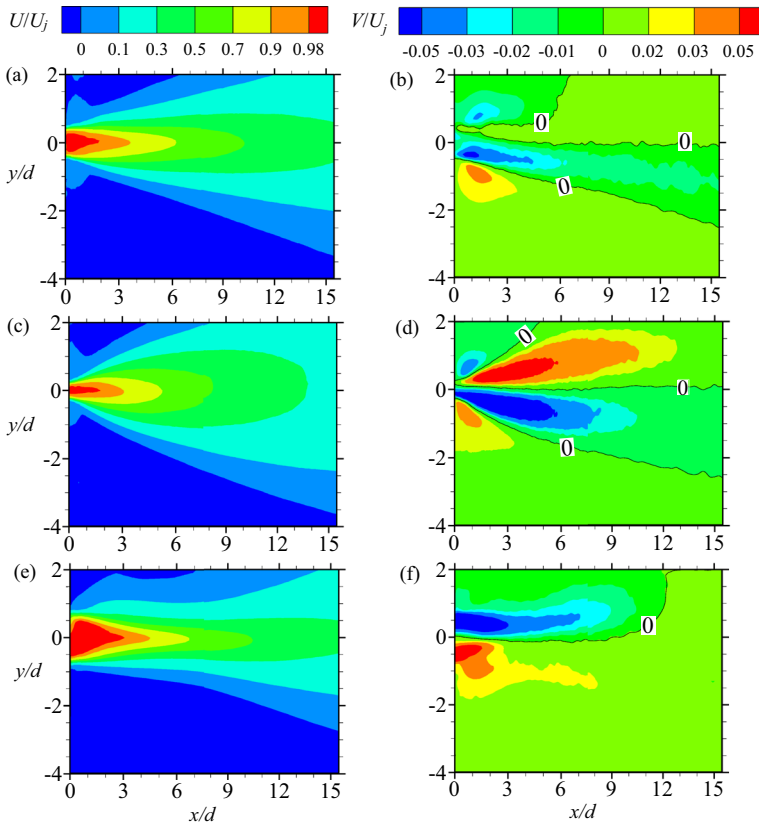


Fig. 5 Iso-contours of streamwise and surface-normal mean velocities: (a) Streamwise mean velocity of square jet, (b) surface-normal mean velocity of square jet, (c) streamwise mean velocity of Rect_minor jet, (d) surface-normal mean velocity of Rect_minor jet, (e) streamwise mean velocity of Rect_major jet, and (f) surface-normal mean velocity of Rect_major jet

The contour plots of the normalized surface-normal mean velocity (V/U_j) are presented in Fig. 5b, d and f for the square, Rect_minor and Rect_major jets, respectively. Line contours of $V/U_j = 0$ are superimposed on the plots to show the demarcation between positive and negative surface-normal mean velocities. As shown in Fig. 5b and d for the square and Rect_minor jets, respectively, V/U_j has both positive and negative distributions in the upper and lower shear layers. This is in concert with the outward spread and fluid entrainment into the jet in both halves of the shear layer. The positive and negative contours in the upper shear layer have a more limited spatial extent than those in the lower shear layer. This is due to the confinement of the shear layer by the free surface that reduces the jet spreading rate and entrainment of ambient fluid. The wider and more elongated V/U_j contours observed for the Rect_minor jet

Table 1 Summary of the potential core length and attachment length for various nozzle geometries

Geometry	L_p/d	L_a/d
Circular	3.0	6.4
Square	2.0	6.4
Rect_minor	2.0	4.8
Rect_major	3.0	7.7

are consistent with the more rapid expansion of the jet in this case compared to the square and circular jets. In the major plane of the rectangular nozzle (Rect_major jet), the contours are predominantly negative in the upper shear layer and positive in the lower shear layer suggesting an initial contraction of the shear layers due to axis-switching.

3.4 Jet deflection, maximum mean velocity decay and spreading rate

The surface attaching jet centerline has a characteristic deflection from the straight direction towards the free surface [1, 8]. Here, the amount of jet deflection was quantified using the parameter y_m , as defined in Fig. 1. Figure 6a shows profiles of y_m/d as a function of streamwise distance in the four jets. The dashed horizontal line at $y_m/d = 0$ indicates the nozzle centerline. For the circular and square nozzles, the deflection y_m/d is negligibly small over most of the measurement region. In these cases, the jet travels almost parallel to the free surface until some ten diameters downstream of attachment before being deflected towards the surface. This is reflective of the comparatively limited jet-surface interaction for these nozzles. For the rectangular nozzle, Rect_minor, the deflection is only negligible within $0 \leq x/d \leq 10$. After attachment, it begins to peel off rapidly away from the axis. The onset of jet deflection is delayed slightly, though, in the major plane of the rectangular jet due to the axis-switching effect. It should be noted that in the interaction region, the deflection is a linear function of x/d . This behaviour was also noted in previous surface attaching jets [1, 8]. As was done in those studies, least-squares lines were fitted to the deflections in the interaction region to measure the rates of jet deflection. The largest deflection rate is observed for Rect_minor, indicated by a slope of $dy_m/dx \approx 0.100$, which is approximately 60% and 73% higher than those measured for the Rect_major ($dy_m/dx \approx 0.040$) and square/circular ($dy_m/dx \approx 0.027$) jets, respectively.

The entrainment and mixing characteristics of turbulent jets are often assessed using the maximum velocity decay and jet spread rate [5, 7, 38]. The effect of nozzle geometry on the streamwise decay of the maximum mean streamwise velocity (U_m) is examined in Fig. 6b. Data obtained from the surface attaching square jet studied by Sankar et al. [20] at offset height, $h/d = 2$, is included for comparison. The maximum mean streamwise velocity normalized by the exit velocity (U_j/U_m) is self-similar and nearly constant in the potential core region ($0 \leq x/d < 3$). Further downstream, U_j/U_m increases almost linearly as U_m is reduced by the entrainment and mixing of the jet. The present square jet shows good agreement with that of Sankar et al. [20]. To estimate the decay rates of the maximum mean streamwise velocity, least-squares lines were fitted to the U_j/U_m profiles according to the relation [39]:

$$U_j/U_m = K_d (x/d - x_k/d) \quad (1)$$

where, K_d and x_k denote the decay rate and kinematic virtual origin, respectively. A summary of the decay rates and the range of streamwise distance over which they were estimated is given in Table 2 for the four geometries. The decay rates of the circular, square and Rect_major jets are comparable. The decay rate of the circular jet is approximately 15% slower than the free circular jet studied by Aleyasin et al. [6] using a similar orifice nozzle at $Re = 17,000$. The slower decay rate of the surface attaching circular jet can be attributed to the reduced entrainment from the upper side of the jet by

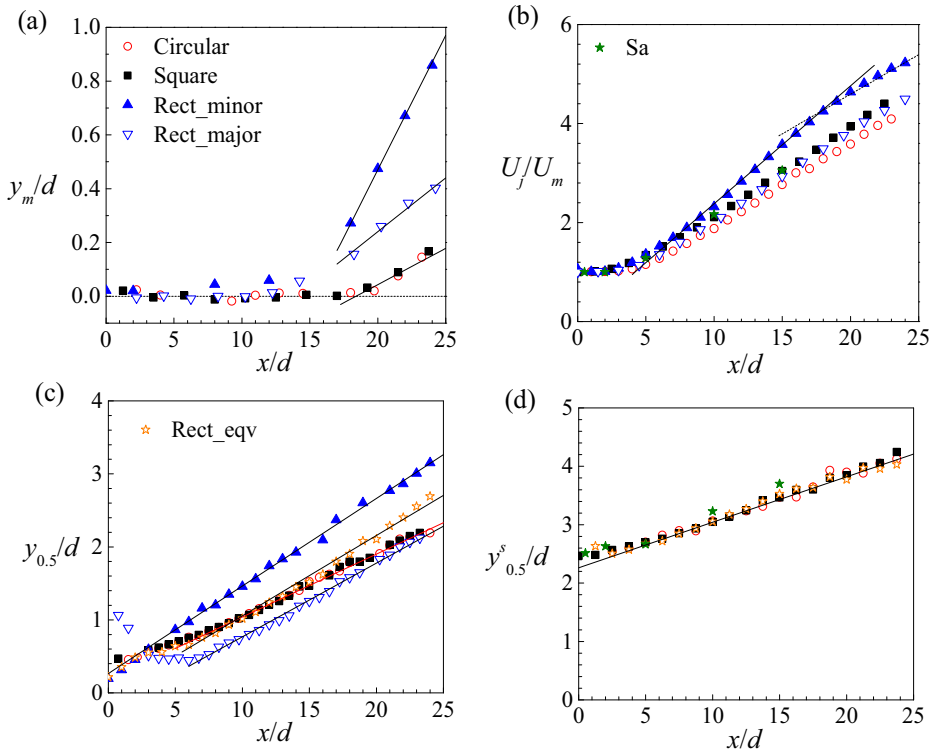


Fig. 6 Streamwise variation of (a) jet deflection, (b) maximum velocity decay, (c) half velocity width measured from the location of U_m , and (d) half velocity width measured from the free surface. Sa = Sankar et al. [20]. The straight lines are least-squares fit on the profiles

the confinement. This effect was also observed in other studies [1, 8]. Compared to the other jets, the Rect_minor jet enhanced the velocity decay rate by a margin of up to approximately 30% within the range $5 \leq x/d \leq 18$. This is consistent with the more rapid expansion, faster spreading and enhanced mixing capability of the Rect_minor jet compared to other configurations. In the far field of the interaction region ($x/d \geq 18$), the Rect_minor decay rate declines by approximately 33%. This is marked by a characteristic change in slope of the decay curve and represents a reduction in entrainment as the jet momentum is used to accelerate the surface flow. Similar far field declines were reported by Madnia and Bernal [1] and Tay et al. [8]. It is worth-noting also that for the

Table 2 Summary of the decay and spread rate for various nozzle geometries

Geometry	K_d (Range)	K_s (Range)
Circular	0.170 ($5 \leq x/d \leq 24$)	0.086 ($5 \leq x/d \leq 24$)
Square	0.176 ($5 \leq x/d \leq 24$)	0.086 ($5 \leq x/d \leq 24$)
Rect_minor	0.238 ($5 \leq x/d \leq 18$), 0.160 ($18 \leq x/d < 24$)	0.120 ($0 \leq x/d \leq 24$)
Rect_major	0.176 ($5 \leq x/d \leq 24$)	0.101 ($6 \leq x/d \leq 24$)
Rect_eqv	–	0.110 ($6 \leq x/d \leq 24$)

Rect_minor jet, the region experiencing diminished rate of maximum mean streamwise velocity decay coincides with that of rapid jet deflection (Fig. 6a), supporting its stronger interaction with the free surface.

Figure 6c shows the profiles of the half-velocity width ($y_{0.5}$), which is often used to quantify the spread rate in turbulent jets. Downstream of the potential core, the spreads of the circular, square and Rect_minor jets are approximately linear. For the Rect_major jet, on the other hand, there is an initial shrinkage of the jet due to the axis-switching effect (occurring near $x/d \approx 2.5$). This reduces the half width in the near field region ($0 \leq x/d \leq 6$) of the Rect_major configuration. Even though the spread of the jet is restored after the initial region, it does not fully recover to that of the Rect_minor jet. This bitonic behaviour of the half-width distribution in the major plane of the rectangular jet is common in asymmetric nozzles oriented in the major axis [6, 7]. To quantify the spread rates of the jets, least-squares straight lines of the form

$$y_{0.5}/d = K_s (x/d - x_g/d) \quad (2)$$

were fitted to the $y_{0.5}$ profiles, where K_s and x_g denote the spreading rate and geometric virtual origin, respectively. The fitted values of the spread rate and their corresponding measurement ranges are summarized in Table 2. The spread rates of the circular and square jets are similar, which speaks to the nearly similar downstream evolution of both jets. These values are comparable to values of $K_s \approx 0.087$ [39] and $K_s \approx 0.088$ [40] reported for free square and round jets, respectively. When using the Rect_minor configuration, however, the spread rate is enhanced by approximately 40% in comparison to the circular and square jets. In the major plane of the rectangular, this enhancement is reduced by approximately 8%. To compare the present Rect_minor and Rect_major jet with a free rectangular jet (Rect_eqv), an equivalent half-velocity width, $(y_{0.5})_{\text{eqv}}$ is estimated as follows:

$$(y_{0.5})_{\text{eqv}} = \sqrt{(y_{0.5})_{\text{minor}} \times (y_{0.5})_{\text{major}}} \quad (3)$$

where $(y_{0.5})_{\text{minor}}$ and $(y_{0.5})_{\text{major}}$ denote the half velocity widths in the minor and major planes of the rectangular jet, respectively. This equivalent half-velocity width corresponds to the shear layer development of an equivalent free rectangular jet. The spread rate of Rect_eqv is intermediate to those of the Rect_minor and Rect_major jets, and it exceeds the spread rate of the circular and square jets by 22%. The higher spread rate of Rect_eqv is consistent with similar rapid growth of rectangular free jets studied in the past [7, 41] compared to circular and square jets. As shown in Fig. 6d, when the half velocity width is measured relative to the free surface ($y^*_{0.5}$), the current profiles and that of Sankar et al. [20] collapse reasonably well on to the same line. The slope of the line was estimated to be approximately 0.078, which is in good agreement with that reported for confined circular jets by Madnia and Bernal [1].

3.5 Surface mean velocity, vorticity thickness and surface turbulence intensities

To characterize the growth of the upper shear layer and its interaction with the free surface, the streamwise mean surface velocity, vorticity thickness and surface turbulence intensities are examined. It is noted that due to a challenge of measuring the data exactly

at the free surface, the data measured about two interrogation area size (≈ 1.5 mm) below the free surface in the PIV image are taken as the surface statistics. Figure 7a shows the profiles of the streamwise mean surface velocity, U_s for the four test conditions. Upstream of the attachment point $U_s \approx 0$; thus, in this figure, the origin of the x axis is shifted by the attachment length, L_a in order to focus the discussion on the interaction region. In all four configurations, the mean surface flow accelerates to a maximum at a streamwise location some ten nozzle widths downstream of the attachment point. Similar observations were reported by Madnia and Bernal [1]. The profiles collapse for the circular, square and Rect_major jets in the interaction region, within the limits of experimental uncertainty. However, the more vigorous expansion of the Rect_minor jet causes a more dramatic increase in U_s compared to the other jets. Farther downstream, this effect is followed by a deceleration of the surface mean flow, albeit to a level that is still substantially higher than the other jets. In the absence of mean surface deformation, the surface mean flow profiles suggest that the free surface is severely strained, due to the alternating acceleration ($\partial U_s / \partial x > 0$) and deceleration ($\partial U_s / \partial x < 0$). This is typically the state of the free surface for confined jets issuing at low offset height ratio from the free surface [1, 8]. The results in Fig. 7a suggest that the free surface is more severely strained in the Rect_minor jet than in the circular, square and Rect_major jets. The profiles have a characteristic “s-shape” with an inflection point ($\partial^2 U_s / \partial x^2 = 0$) at $(x-L_a)/d \approx 6$. This is not dissimilar to the inflection point in the velocity profile of mixing layers where the turbulent activity reaches a maximum.

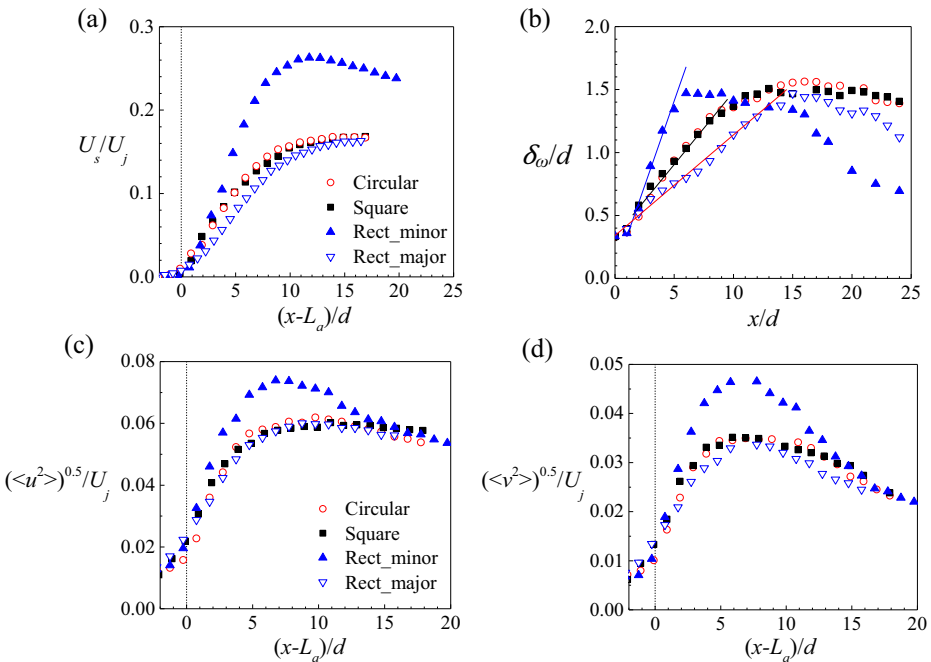


Fig. 7 Streamwise variation of (a) streamwise mean surface velocity, (b) vorticity thickness, (c) streamwise surface turbulence intensity and (d) surface-normal surface turbulence intensity. The solid lines in (b) are the least-squares linear fit

Figure 7b compares the streamwise evolution of the vorticity thickness, δ_ω , in the four jets. The vorticity thickness is often used to investigate the growth of the shear layer [42]. The values of δ_ω were estimated as

$$\delta_\omega = \frac{\Delta U}{(\partial U / \partial y)_{\max}} \quad (4)$$

where, $\Delta U = U_m - U_s$ and $(\partial U / \partial y)_{\max}$ is the maximum mean strain rate in the upper shear layer. The vorticity thickness grows almost linearly with streamwise distance before the jet-surface interaction indicating a streamwise growth of the vortices generated in near field region.

The vorticity thickness values of the circular and square nozzle are quasi-similar over the entire range of measurement. This implies that the vortices generating the turbulence in both jets are structurally similar. The growth rate, $d\delta_\omega/dx$, of the vorticity thickness was estimated as the slope of the least-squares line fitted to the data. The calculations yielded the growth rate values of approximately 0.115 for the circular and square jets; 0.270 for Rect_minor jet and 0.080 for the Rect_major jet. About 57% rapid growth rate in the minor plane of the rectangular nozzle than the circular jet, and 30% lesser in the major plane of the rectangular nozzle than the circular one are consistent with the expansion of the shear layers in the near field region. The vorticity thickness is not a well-documented parameter for surface attaching jets. However, the present values from the circular, square and Rect_minor jets are within the range of 0.110–0.270 reported in the literature for a wide variety of turbulent shear flows, including mixing layers [43], separated and reattached shear layers over forward facing steps [44, 45], backward facing steps [46, 47], and two-dimensional cavities [48, 49]. In the interaction region, the free surface limits the growth of the upper shear layer, causing δ_ω to remain relatively constant up to some ten nozzle widths downstream of the attachment point. This is noticeable within $5 < x/d < 15$ for the Rect_minor jet and within approximately $10 < x/d < 20$ for the square and circular jets. The plateau is absent for the Rect_major jet because the axis-switching in this jet will continue the growth of the structures over a larger streamwise distance than the other jets. The relatively constant values of δ_ω would suggest that within the early parts of the interaction region of the circular, square and Rect_minor jets the surface-normal scale of the vortices is approximately constant. Farther downstream, a characteristic decay of the δ_ω values occur, which can be partly attributed to shrinkage of the vorticity field in the upper shear layer as the jet deflects towards the free surface.

Figure 7c and d show the profiles of the streamwise and surface-normal turbulence intensities, respectively, along the free surface. The surface turbulence intensities increase rapidly in the early interaction region, reaching peak values at a streamwise location approximately six nozzle widths downstream of the attachment point. The location of the peak values corresponds to the inflection point in the surface mean streamwise velocity profile. The surface turbulence intensities from the circular, square and Rect_major jets compare fairly well. However, the larger mean strain imposed on the free surface by the rapidly expanding Rect_minor jet produces a hump in the turbulence intensity profiles. The peak values of the streamwise and surface-normal turbulence intensities in Rect_minor are approximately 19% and 24% larger than in the other geometries, respectively. In the far downstream region, the surface turbulence intensities decay to levels that are independent of nozzle geometry. In all cases, the surface-normal turbulence intensity is significantly lower than the streamwise counterpart. This is an indication of strong anisotropy of the Reynolds stress field at the free surface. The results also reveal that there is a more dramatic far field decay in the surface-

normal turbulence intensity than the streamwise turbulence intensity. As noted in previous investigations [10, 18], this is consistent with the damping of the surface-normal velocity fluctuations by the free surface.

3.6 Effects of nozzle geometry on the surface-normal profiles of mean velocity and Reynolds stresses

Figure 8 examines the effects of nozzle geometry on one-dimensional profiles of the mean velocity and Reynolds stresses at selected streamwise locations ($x/d = 10, 15, 24$) in the interaction region. The surface-normal distance is normalized by the offset height, h . With $h (= 2d)$, the free surface is now located at $y/h \approx 1$. Figure 8a shows that the streamwise mean velocity profiles, U/U_m . At $x/d = 10$, the mean velocity profile of the Rect_major jet is almost Gaussian because of the delayed onset of interaction between its upper shear layer and the free surface. For the square and Rect_minor configuration, the upper shear layer is travelling much faster than the lower shear layer. This persists throughout the interaction region, resulting in increasingly large U/U_m at the free surface, or in a motion of surface current. Throughout the interaction region, the upper shear layer of Rect_minor is accelerating the fastest, while that of Rect_major catches up to the square jet. In the lower shear layer, the disparities

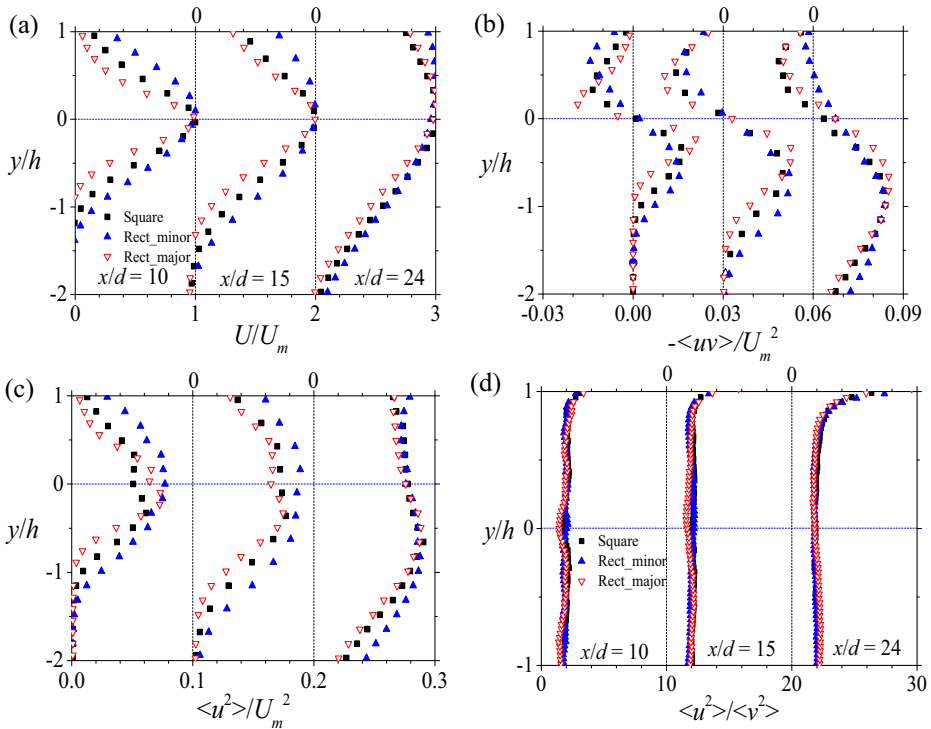


Fig. 8 Surface-normal profiles of mean velocity and Reynolds stresses for square, Rect_minor and Rect_major jet at the selected x/d locations: (a) Streamwise mean velocity, (b) Reynolds shear stress, (c) streamwise Reynolds normal stress, and (d) stress ratio

between the profiles become negligibly small in the far field region. The accelerating U/U_m has the effect of flattening the velocity profile in the upper shear layer. This causes a progressive decrease in the surface-normal gradient of the mean velocity ($\partial U/\partial y$) in the interaction region.

Figure 8b shows profiles of the Reynolds shear stress, $-\langle uv \rangle/U_m^2$ in the interaction region. At $x/d \approx 10$, the peak values of $-\langle uv \rangle/U_m^2$ in the square and Rect_minor jets are comparable but are approximately 26% lower than peak values for the Rect_major jet in both halves of the shear layer. The locations of the peak Reynolds shear stress in Rect_major are closer to the centerline ($y/h = 0$) than in the square and Rect_minor jets because of the slower growth rate of the Rect_major jet. With increasing streamwise distance, the peak Reynolds shear stress in the upper shear layer decreases as the mixing zone shrinks under the influence of confinement. The effect is most dramatic for the Rect_minor jet in comparison to the other jets. This can be explained by the increasingly flat shape of the mean velocity profile and the corresponding rapid decay of the mean strain rate $\partial U/\partial y$ as the jet evolves downstream. On the other hand, as the lower shear layer evolves, the corresponding peak values of $-\langle uv \rangle/U_m^2$ persistently increase, but these are not affected by differences in nozzle geometry. The effect of nozzle geometry in the lower shear layer is seen in the widening area of the zone of significant Reynolds shear stress. The results indicate enhancements of the Reynolds shear stress for Rect_minor in the mixing region of the lower shear layer.

Figure 8c shows the profiles of the streamwise Reynolds normal stress, $\langle u^2 \rangle/U_m^2$. In the interaction region, the profiles from square and Rect_major jets are comparable, except at $x/d \approx 10$ where the centerline values of $\langle u^2 \rangle/U_m^2$ were enhanced by 20% by the Rect_major configuration in comparison to the square jet. The minor-axis orientation of the rectangular jet causes substantial enhancements in $\langle u^2 \rangle/U_m^2$ away from the centerline for most of the interaction region. The profiles exhibit the presence of significant turbulent activity near the free surface, while $\langle u^2 \rangle/U_m^2$ is growing with streamwise distance. It is noted that the profiles of surface-normal Reynolds normal stress, $\langle v^2 \rangle/U_m^2$ (not shown herein) exhibit similar trend but with a lower magnitude compared to $\langle u^2 \rangle/U_m^2$ close to the free surface, irrespective of nozzle geometry. This demonstrates the strong anisotropy of the Reynolds normal stresses, both at the free surface and within the jets. To explore the anisotropy of the Reynolds normal stresses, values of the anisotropy parameter $\langle u^2 \rangle/\langle v^2 \rangle$ was calculated. Figure 8d shows the profiles of the stress ratio $\langle u^2 \rangle/\langle v^2 \rangle$ in the interaction region. The plots indicate that $\langle u^2 \rangle/\langle v^2 \rangle \approx 2$ within the shear layers. At the free surface, the stress ratio is larger and grows with streamwise distance as the impact of the interaction becomes stronger. This high level of anisotropy in the Reynolds normal stresses suggests that RANS (Reynolds-averaged Navier–Stokes) models such as standard two-equation models (e.g., $k-\varepsilon$ model, $k-\omega$ model), that employ the isotropic assumption cannot reproduce the correct level of the Reynolds normal stresses measured in the interaction region. Instead, second moment closures that directly computes the Reynolds stresses will be required to predict the flow adequately.

3.7 Two-point spatial correlations

Distributions of the two-point spatial correlations were calculated in order to investigate the effects of nozzle geometry on the average spatial dimensions of the large-

scale coherent structures in the interaction region. The two-point spatial correlation between any two quantities $A(x, y)$ and $B(x, y)$ at the reference location (x_{ref}, y_{ref}) is defined as

$$R_{AB}(x_{ref} + \Delta x, y_{ref} + \Delta y) = \frac{\langle A(x_{ref}, y_{ref})B(x_{ref} + \Delta x, y_{ref} + \Delta y) \rangle}{\sigma_A(x_{ref}, y_{ref})\sigma_B(x_{ref} + \Delta x, y_{ref} + \Delta y)} \quad (5)$$

where, Δx and Δy are the spatial separations between A and B in the streamwise and surface-normal directions, respectively; σ_A and σ_B are the root-mean-square values of A and B at (x_{ref}, y_{ref}) and $(x_{ref} + \Delta x, y_{ref} + \Delta y)$, respectively, and the quantity with the symbol “ $\langle \rangle$ ” represents the covariance of A and B . Figure 9 shows the surface-normal evolution of the two-point auto-correlation function of the streamwise velocity fluctuation, R_{uu} at a location of $x/d = 20$ in the interaction region. The surface-normal locations, measured relative to the free surface, correspond to the y -locations, $y_s/d = 0.5, 1.0$ and 3.0 , the first two of which are in the upper shear layer and the third is in the lower shear layer. It is noted that the correlation function typically exhibits a sign change from positive to negative beyond some finite distance from the reference location [14, 17]. However, the current field of view was not large enough to capture the whole structure at this particular streamwise location and missed the negative correlation features. Therefore, a minimum correlation level of up to $+0.3$ is shown in the figure for all of the nozzle geometries for consistency. The most defining characteristic of R_{uu} is that the contours of the correlation functions are profoundly elongated in the streamwise direction. At $y_s/d = 0.5$, the contours of the correlation function are still attached to the free surface. This provides evidence of large-scale structures near the free surface that have been ejected from the jet [1, 18]. The attached contours have relatively shallow streamwise inclination angles of approximately $12^\circ \pm 1.5^\circ$. These values are consistent with the value of approximately 11° reported for wall jets [50] and zero pressure gradient turbulent boundary layers [51]. At larger distances from the free surface, the extent of significant R_{uu} correlation, as well as the streamwise inclination angle of the contours are decreasing. In the upper shear layer, the Rect_minor configuration decreases the spatial dimensions of the contours relative to the square jet. The Rect_major jet enhances the correlation in relation to the Rect_minor jet. At $y_s/d = 3.0$, the contours are almost parallel to the free surface because of the reduced influence of the free surface in the lower shear layer. Also, Rect_minor has no perceptible influence on the correlation here in comparison to the square jet. However, re-orientation of the nozzle causes enhancements in the correlation with respect to the Rect_minor orientation.

Figure 10 shows the contours of the spatial auto-correlation function of the surface-normal velocity fluctuation, R_{vv} . Similar to R_{uu} , contour levels are shown from the self-correlation peak to a minimum contour level of $+0.3$ irrespective of nozzle geometries. The contours are elongated in the surface-normal direction and attached to the free surface for reference locations close to the free surface. Near the free surface, the Rect_minor nozzle causes a more pear-shaped surface-normal auto-correlation in comparison to the other configurations. This is due to the more rapid damping of the surface-normal velocity fluctuations near the free surface in the Rect_minor case. At larger distances from the free surface, the R_{vv} contours show the opposite trend to that of R_{uu} , which consists of enhanced growth with distance away from the free surface. This growth persists into the lower shear layer and is indicative of the reduced damping of the surface-normal velocity fluctuations. The most dramatic enhancements occur in the Rect_major jet, both in the upper and lower shear layer. An enhancement of the R_{uu} and R_{vv} correlations in the far field of the Rect_major jet compared to the other configurations signifies

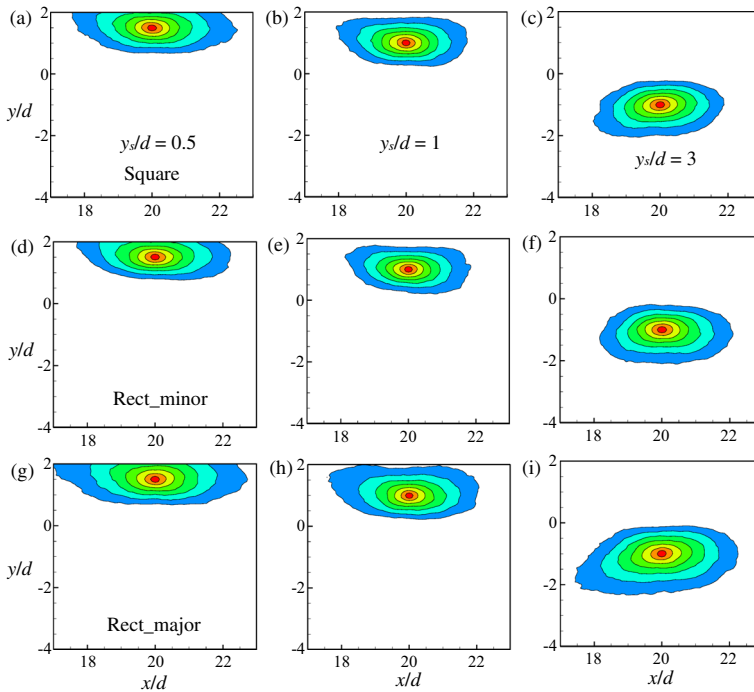


Fig. 9 Iso-contours of R_{uu} for square, Rect_minor and Rect_major jet at various surface-normal locations at $x/d = 20$: (a) Square jet at $y_s/d = 0.5$, (b) square jet at $y_s/d = 1$, (c) square jet at $y_s/d = 3$, (d) Rect_minor jet at $y_s/d = 0.5$, (e) Rect_minor jet at $y_s/d = 1$, (f) Rect_minor jet at $y_s/d = 3$, (g) Rect_major jet at $y_s/d = 0.5$, (h) Rect_major jet at $y_s/d = 1$ and (i) Rect_major jet at $y_s/d = 3$. Contour levels vary from 0.3 to 0.9 at intervals of 0.1

the presence of more energetic large-scale structures in far field of Rect_major. This can be partly considered as an artifact of restoring the shear layer development for Rect_major jet after the axis-switching. It also points to the Rect_major orientation as a more plausible choice for mixing enhancement in the far field region over the square and Rect_minor jets. It is noted that in case of an overall better mixing performance in both the near and far fields, Rect_minor jet can be a better choice as it starts with the most enhanced mixing in the near and intermediate field ($0 \leq x/d \leq 18$) considering its faster maximum velocity decay and spread rates.

To quantify the average spatial dimensions of the structures along the jet centerline, the streamwise and surface-normal extents of the two-point auto-correlations, R_{uu} and R_{vv} , were estimated. Following Tay et al. [8], the streamwise and surface-normal extents are estimated as the distance from the self-correlation peak to the minimum correlation level of +0.3 in the streamwise and surface-normal direction, respectively. The streamwise evolution of the streamwise extents of R_{uu} and R_{vv} ($L_{x,uu}$ and $L_{x,vv}$, respectively); and the surface-normal extents of R_{uu} and R_{vv} ($L_{y,uu}$ and $L_{y,vv}$, respectively) for the four nozzle geometries are shown in Fig. 11. The collapse of these profiles along the jet centerline suggests that the significant effect of nozzle geometry on the turbulent structures observed in the vicinity of the free surface, as discussed in Figs. 9 and 10, is negligible on the jet centerline. Similar independency of the nozzle geometry on the integral length scales was reported for free jets [17]. After the potential core region ($x/d > 3$), the profiles increase almost linearly with x/d due to characteristic increase of the size of the large-scale structure with the streamwise growth of the shear layer [17]. The

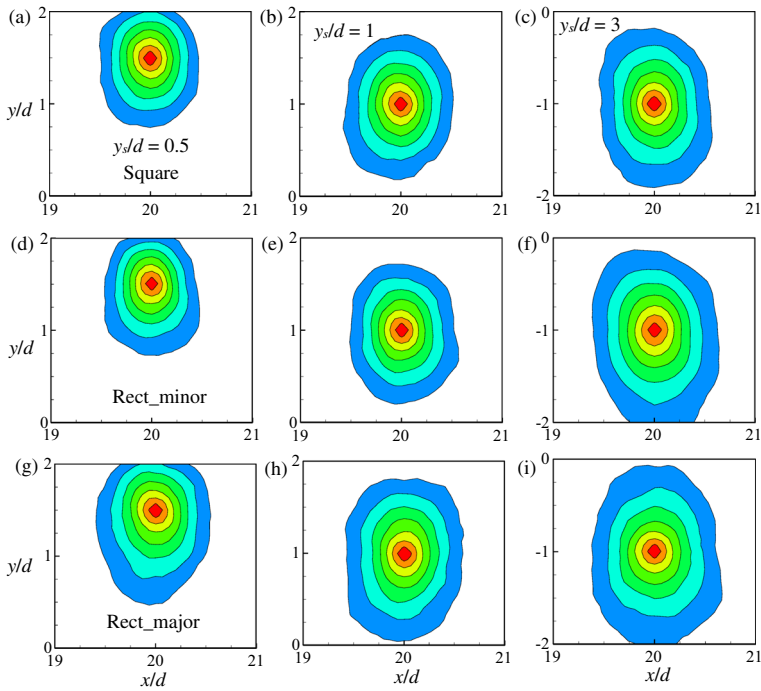


Fig. 10 Iso-contours of R_{vv} for square, Rect_minor and Rect_major jet at various surface-normal locations at $x/d = 20$: (a) Square jet at $y_s/d = 0.5$, (b) square jet at $y_s/d = 1$, (c) square jet at $y_s/d = 3$, (d) Rect_minor jet at $y_s/d = 0.5$, (e) Rect_minor jet at $y_s/d = 1$, (f) Rect_minor jet at $y_s/d = 3$, (g) Rect_major jet at $y_s/d = 0.5$, (h) Rect_major jet at $y_s/d = 1$ and (i) Rect_major jet at $y_s/d = 3$. Contour levels vary from 0.3 to 0.9 at intervals of 0.1

linear growth rate of $L_{x,uu}$ (Fig. 11a) is estimated as 0.057, which is about 70% higher than the slope of 0.017 for $L_{x,vv}$ (Fig. 11b) indicating a major role of streamwise velocity fluctuation than the surface-normal component in streamwise stretching of the large-scale structure. Because the free surface limits the surface-normal growth of the structures, it was considered important to verify whether the surface-normal extents $L_{y,uu}$ (Fig. 11c and e) and $L_{y,vv}$ (Fig. 11d and f) grow uniformly on either side of the self-correlation peak. In the initial region, the about 30% reduced $L_{y,uu}$ can be partly attributed to reduced fluctuating velocity as the potential core region is mainly dominated by the mean flow. Afterwards, the linear growth rate of $L_{y,uu}$ is estimated as 0.025 in both the upper (Fig. 11c) and lower shear layers (Fig. 11e) implying negligible effect of the free surface on the surface-normal extent of R_{uu} . For R_{vv} , the surface-normal extent increases at a similar rate as $L_{y,uu}$ in the upper shear layer (Fig. 11d), which increases to 0.042 in the lower shear layer (Fig. 11f). Slower growth rate of $L_{y,vv}$ in the upper shear layer (approximately 40%) can be considered as an artefact of damping effect of the free surface on the surface-normal velocity fluctuation correlation. It is noted that the present growth rate of $L_{x,uu}$ and $L_{y,uu}$ are approximately 26% higher and lower, respectively compared to a free jet by Aleyasin et al. [17], where contoured nozzle was used. The discrepancy can be partly attributed to different initial and boundary conditions, such as the enhanced mixing by an orifice type nozzle used in the present study than a contoured nozzle [28] that leads to higher expansion of the shear layer, while the surface confinement restricts the surface-normal growth of large-scale structure.

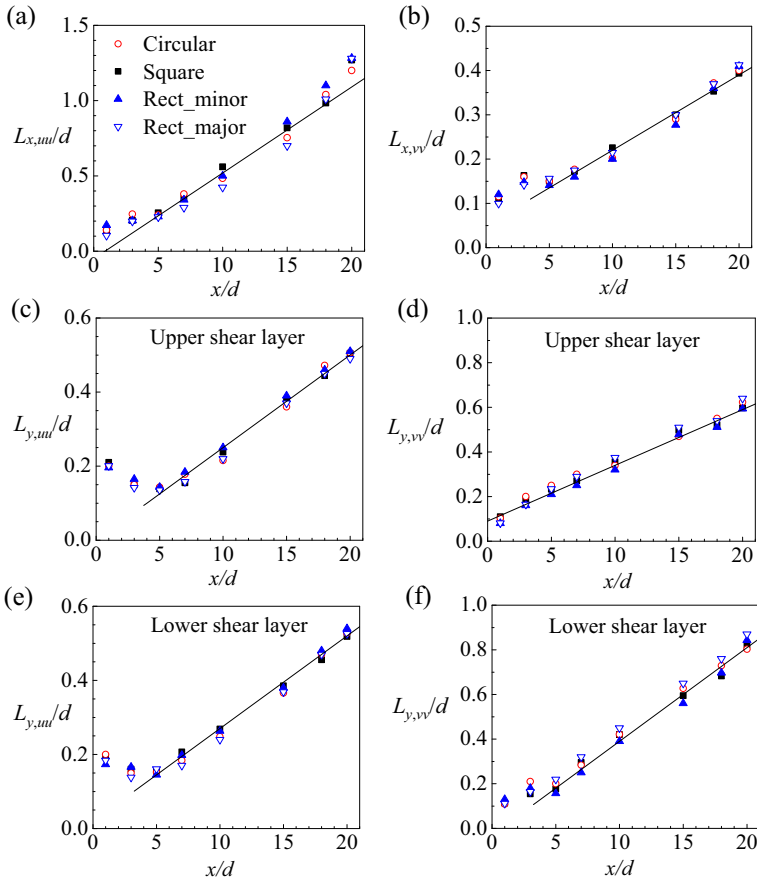


Fig. 11 Variation of the integral scales of the auto-correlation functions with streamwise distance for various nozzle geometries along the jet centerline: (a) Streamwise integral scale of R_{uu} , (b) streamwise integral scale of R_{vv} , (c) surface-normal integral scale of R_{uu} in the upper shear layer, (d) surface-normal integral scale of R_{vv} in the upper shear layer, (e) surface-normal integral scale of R_{uu} in the lower shear layer and (f) surface-normal integral scale of R_{vv} in the lower shear layer. Solid lines are least-squares linear fit

Figures 12 and 13 show the contours of the two-point cross-correlations between the swirling strength, and the streamwise and surface-normal velocity fluctuations ($R_{\lambda u}$ and $R_{\lambda v}$, respectively). These correlations are plotted here to provide an indication of the average spatial extent and strength of the velocity fields associated with the circumferential vortex rings. Using the Galilean decomposition method, these vortices were revealed to be pre-dominantly retrograde vortex cores in the upper shear layer and prograde vortex cores in the lower shear layer. The iso-contours of $R_{\lambda u}$ presented in Fig. 12 reveal retrograde vortices at the reference locations in the upper shear layer ($y_s/d = 0.5$ and 1.0). These are identified by the negative $R_{\lambda u}$ above the reference location and positive $R_{\lambda u}$ beneath the reference location. The correlations were also able to detect the corresponding prograde vortices in the lower shear layer that are on the same helical ring as those in the upper shear layer. With increasing distance from the surface, the negative correlations are strengthened because there is less damping of the spanwise vortex cores. This holds true for the square and Rect_major jets. For the Rect_minor jet, however, the spatial coherence of the velocity field around the reference location is disrupted. This reflects reduced population density of swirling strength at

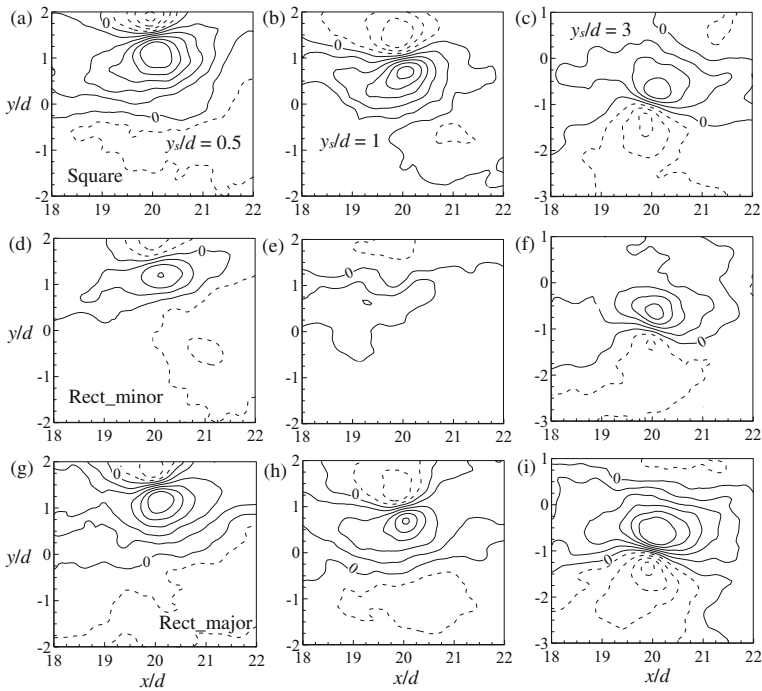


Fig. 12 Iso-contours of $R_{\lambda u}$ for square, Rect_minor and Rect_major jet at various surface-normal locations at $x/d = 20$: (a) Square jet at $y_s/d = 0.5$, (b) square jet at $y_s/d = 1$, (c) square jet at $y_s/d = 3$, (d) Rect_minor jet at $y_s/d = 0.5$, (e) Rect_minor jet at $y_s/d = 1$, (f) Rect_minor jet at $y_s/d = 3$, (g) Rect_major jet at $y_s/d = 0.5$, (h) Rect_major jet at $y_s/d = 1$ and (i) Rect_major jet at $y_s/d = 3$. Contour levels vary from -0.1 to 0.1 at intervals of 0.02 . Dashed contours indicate the negative correlation

the jet centerline, which deflects (see Fig. 6a) and moves close to the reference location. With the increase of y_s/d , the upstream inclination angle of the contours decreases from 84° to 80° for square and 77° to 75° for Rect_major jet. The decrease of the inclination angle as the reference location approaches the centerline is consistent with previous jet study by Tay et al. [8]. For Rect_minor, this angle is 78° at $y_s/d = 0.5$, but it is not estimated at $y_s/d = 1.0$ due to lack of correlation. In the lower shear layer ($y_s/d \approx 3$), prograde vortices are detected at the reference location, indicated by positive $R_{\lambda u}$ above the reference location and negative $R_{\lambda u}$ beneath the reference location. For the square and Rect_major jets, a small negative $R_{\lambda u}$ correlation is captured in the upper shear layer, which corresponds to the retrograde vortex in the same helix as the prograde vortex. In the lower shear layer, the correlation contours are inclined relative to downstream at approximately 71° , 84° and 77° , for the square, Rect_minor and Rect_major jets, respectively.

In Fig. 13, the contours of the two-point correlation between the swirling strength and surface-normal velocity fluctuation, $R_{\lambda v}$, support the flow pattern around a retrograde vortex at $y_s/d = 0.5$ and 1.0 . The contours show enhancement with distance away from the free surface for the square and Rect_major jets but rapid decorrelation in case of the Rect_minor jet like the $R_{\lambda u}$ result. In the upper shear layer, the contours of the square and Rect_major jets exhibit slight inclinations of approximately 7° to the upstream direction. This inclination angle is reduced to approximately zero in the Rect_minor jet. In the lower shear layer, the contours are reversed and support the velocity field pattern around a prograde vortex. The contours are inclined at angles of approximately 7° , 5° and 12° for the square, Rect_minor and Rect_major jets, respectively.

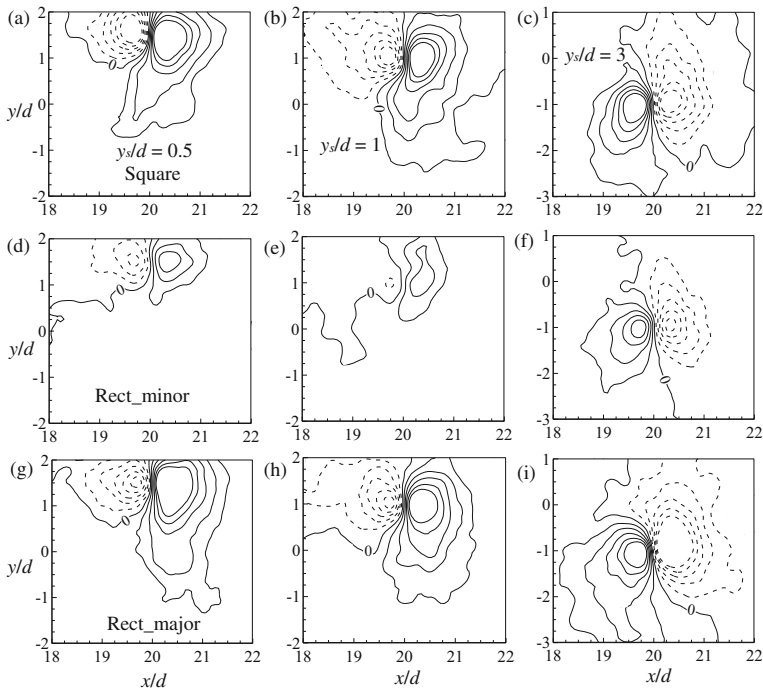


Fig. 13 Iso-contours of $R_{\lambda v}$ for square, Rect_minor and Rect_major jet at various surface-normal locations at $x/d = 20$: (a) Square jet at $y_s/d = 0.5$, (b) square jet at $y_s/d = 1$, (c) square jet at $y_s/d = 3$, (d) Rect_minor jet at $y_s/d = 0.5$, (e) Rect_minor jet at $y_s/d = 1$, (f) Rect_minor jet at $y_s/d = 3$, (g) Rect_major jet at $y_s/d = 0.5$, (h) Rect_major jet at $y_s/d = 1$ and (i) Rect_major jet at $y_s/d = 3$. Contour levels vary from -0.1 to 0.1 at intervals of 0.02 . Dashed contours indicate the negative correlation

3.8 Proper orthogonal decomposition

The proper orthogonal decomposition (POD) method was used to investigate the low-order dynamics of the jets. The snapshot approach of the POD analysis introduced by Sirovich [52] is applied in the present study. A brief description of the method is reported by Nyantekyi-Kwakye et al. [53] and is, therefore, not repeated here. To ensure that enough snapshots were used in the POD, a convergence study was conducted to determine the number of snapshots necessary to capture the largest fraction of the turbulent kinetic energy (TKE). The percentage contributions of the most dominant POD mode (the first mode) were calculated for different numbers of snapshots ($300 \leq N \leq 5000$). It was found that for all nozzle geometries the fractional energy of the first POD mode converged to within 0.1% for $N \geq 4000$, suggesting 5000 snapshots used in this study is sufficient for the POD analysis. Figure 14 shows the profiles of the fractional and cumulative energy fractions calculated for the first 50 modes in Plane 1 ($0 \leq x/d \leq 7$) and Plane 3 ($17 \leq x/d \leq 24$) of the four nozzle configurations. The variation of fractional energy with mode number follows an exponential decay. Similar exponential decay of the fractional energy of the POD modes has been reported in previous free jets [17] and wall attaching jets [53]. In Plane 1 (Fig. 14a), the fractional energy of the first POD mode is nearly independent of nozzle geometry (about 2.7% for circular and Rect_major jet; and 2.3% for square and Rect_minor jet), which is consistent with the self-similarity of the integral length scales in the near field region. In the succession up to mode number 10, there is approximately up to 27% reduction in modal energy

for the non-circular jets in comparison to the circular jet. This can be partly attributed to the breakdown of the large-scale structures in the non-circular jets, introduced by the non-uniform curvature of the exit perimeter. With increasing mode order, the fractional energies collapse and decay rapidly, reaching less than approximately 0.3% by the 50th mode. The profiles of the fractional energy measured in Plane 3 are shown in Fig. 14b. In Plane 3, the fractional energy contributions of the first POD mode are about 4 to 5 times as large as those in Plane 1, suggesting the presence of more energetic eddies in the interaction region than in the near field region. This result is consistent with the increasing size of the length scales in the interaction region as larger spatial coherence of the correlation function was found in the most energetic modes in a previous jet study [54]. In Plane 3, the major-axis orientation of the rectangular nozzle causes an approximately 21% increase in the first mode in comparison to the other nozzles, which is consistent with the larger contour size of the two-point correlation within the shear layers. With increasing mode order, the profiles collapse onto a single exponential curve. Compared to Plane 1, the results indicate a more rapid modal energy decay in Plane 3, which would imply a faster convergence of the POD basis set in this case than in Plane 1. Similar observations were reported in previous free and wall attaching jet studies [17, 53]. The variation of the cumulative energy with mode order in Plane 1 and Plane 3 are shown in Fig. 14c and d, respectively. In Plane 1, the results indicate that in order to capture the same amount of total turbulent kinetic energy, a smaller number of lower-order POD modes is required in the circular jet than in the square, Rect_minor and Rect_major jets. For instance, to capture approximately 30% of the total energy in Plane 1, this requires the first $m = 32$ low-order modes as compared to $m = 36$ for the square and Rect_major jets; and $m = 42$ for the Rect_minor jet. These values are indicative of the energy convergence rate of each POD. A comparably faster convergence for circular jet can be attributed

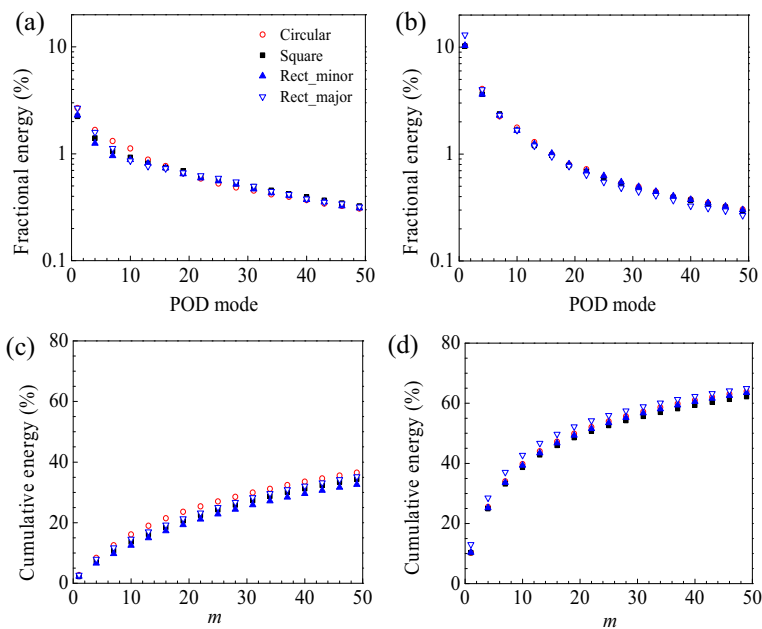


Fig. 14 Variation of fractional and cumulative energy with the mode numbers for various nozzle geometries: (a) Fractional energy in Plane 1, (b) fractional energy in Plane 3, (c) cumulative energy in Plane 1 and (d) cumulative energy in Plane 3

to higher energy content in the lower order modes as mentioned earlier. In the interaction region in Plane 3, even fewer modes are required to capture the same 30% of the total TKE: roughly 6 low-order modes for the various test cases. The reduced number of low-order modes in the interaction region is indicative of faster energy convergence, and by inference, larger eddies in this region compared to the near field region. This is consistent with similar rapid energy convergence in the far field region of free jets [17] and wall attaching jets [53]. The profiles show good agreement among the circular, square and Rect_minor jets but about up to 9% higher values for the Rect_major jet, which can be attributed to higher fractional energy content in the first mode.

To provide insight into the spatial structure of the individual POD modes in the interaction region, vector plots of the eigenfunctions in Plane 3 are examined. Figure 15 shows the vector plots of the 1st, 3rd, 5th and 10th POD modes for the square jet. The 1st POD mode presents the appearance of a massive negative (clockwise rotating) vortex with the jet centerline as its axis. For the higher-order modes, the spatial fields are characterized by two or more randomly arranged spanwise vortex cores with a noticeable downward bent relative to the free surface. This characteristic bent away from the free surface can be attributed to the confinement imposed on the jet. The plots also show spanwise vortices with alternating directions of rotation within the shear layers. This suggests that the higher order modes are responsible for the flow dynamics of the smaller-scale counter-rotating spanwise vortex cores. Qualitatively similar results were reported in POD of surface attaching jet [23, 24, 55] and wall attaching jet [53] that showed that the spatial POD modes govern the development of the shear layer vortices. Figure 16 shows the vector plots of the 1st, 3rd, 5th and 10th POD modes for the Rect_minor and Rect_major jets. There is a marked difference between the mode 1 spatial distributions for the Rect_minor and Rect_major jets: the upper shear layer of the Rect_minor jet does not show any circulation, while that of the Rect_major jet shows flow circulation corresponding to that of a negative (clockwise) vortex. There is no large-scale flow circulation in the upper shear layer of Rect_minor because most of the energy in the shear layer

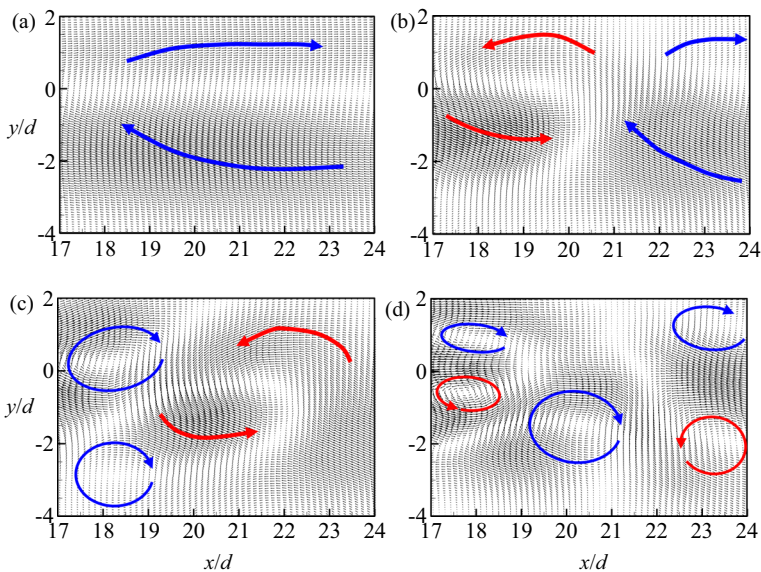


Fig. 15 Vector plots of the POD modes for square jet in Plane 3: (a) mode 1, (b) mode 3, (c) mode 5 and (d) mode 10. mode 1, 3, 5 and 10 contain about 10%, 5.0%, 3.1% and 1.7% of the total energy

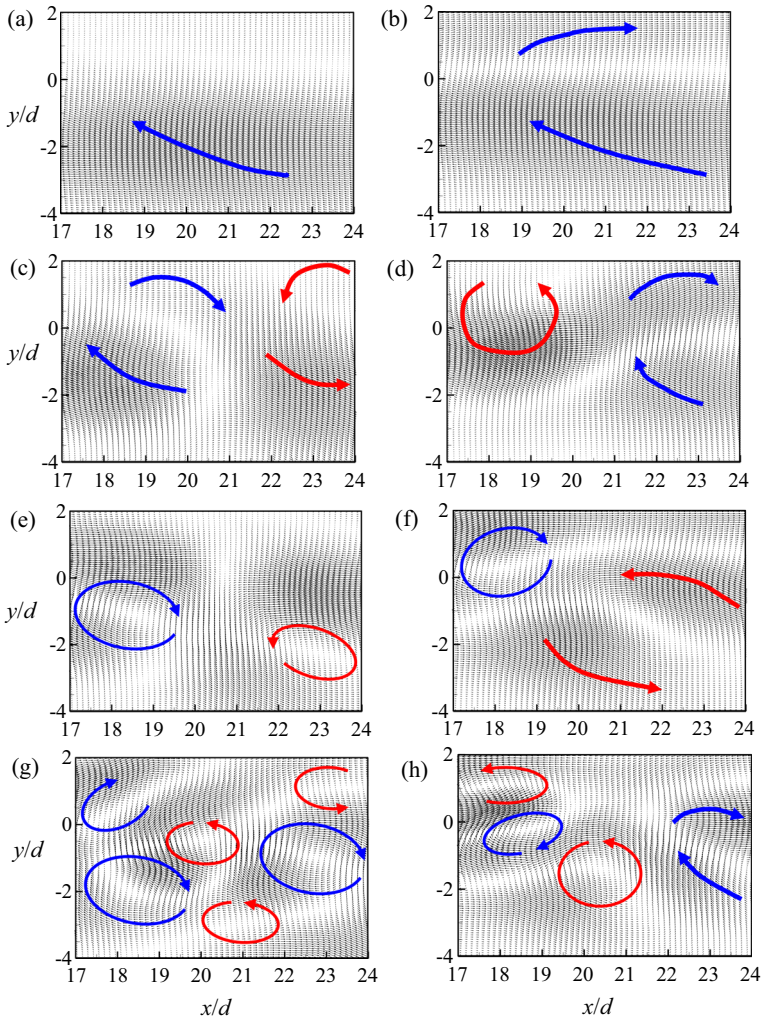


Fig. 16 Vector plots of the POD modes for rectangular jets in Plane 3: (a) mode 1 for Rect_minor, (b) mode 1 for Rect_major, (c) mode 3 for Rect_minor, (d) mode 3 for Rect_major, (e) mode 5 for Rect_minor, (f) mode 5 for Rect_major, (g) mode 10 for Rect_minor and (h) mode 10 for Rect_major jet. Mode 1, 3, 5 and 10 contain about 10%, 4.8%, 3.2% and 1.7% of the total energy, respectively for Rect_minor jet; and 13%, 5.3%, 3.6% and 1.7% of the total energy, respectively for Rect_major jet

is used to drive the surface current. For the higher-order modes, the alternating positive and negative vortices occur but they show no systematic dependency on nozzle geometry or orientation of the rectangular nozzle.

4 Conclusions

A high-resolution particle image velocimetry (PIV) was used to measure the effects of nozzle exit geometry on the flow characteristics and turbulence structure of surface attaching jets.

Detailed velocity measurements were performed for three different types of nozzle exit geometry, including a square, a circular and a rectangular nozzle. For each geometry, the nozzle offset height ratio (h/d) and exit Reynolds number were approximately 2 and 5500, respectively.

Instantaneous flow visualization in the vertical symmetry plane of the jets reveals that due to the more vigorous near field expansion of the jet, the large-scale structures grow more rapidly in the minor plane of the rectangular nozzle than the circular and square nozzles. In the major plane of the rectangular nozzle, the growth of the structures is inhibited initially by the axis-switching of the jet.

The mean velocity contours show that the non-circular nozzles shorten the potential core length (approximately 33%) relative to the circular nozzle. The circular and square nozzles attach at almost similar locations ($L_a/d = 6.4$) near the free surface but the rectangular nozzle in minor-axis orientation reduces the attachment length of about 25%. In the major-axis orientation, the rectangular nozzle increases the potential core (approximately 33%) and attachment length (approximately 38%) when compared to the minor-axis orientation of the nozzle. These results are an indication of more intense near field mixing and entrainment in the minor plane of the rectangular jet. The rapid expansion of the jet in the minor plane of the rectangular nozzle also causes a faster (approximately 60% and 73% than Rect_major and circular/square jet, respectively) deflection of the jet towards the free surface. This is accompanied by the fastest rates of the decay (up to 30%) in the corresponding maximum streamwise mean velocity.

As the jets expand, the upper shear layer interacts with the free surface. Due to the interaction, the characteristic strain on the free surface is more intense for the rectangular jet with minor axis orientation compared to other nozzles. This configuration also enhances the growth of the vorticity thickness in the near field region. Furthermore, the damping of the surface-normal velocity fluctuations at the free surface is more severe in the minor plane of the rectangular jet.

Surface-normal profiles of the single-point turbulent statistics exhibit dependency on nozzle geometry and orientation. The rectangular nozzle in minor axis orientation enhances the mean velocity and streamwise Reynolds normal stress in the upper and lower shear layers relative to the square nozzle and the major-axis counterpart. The differences diminish with increasing downstream distance. On the other hand, the effect of the free surface is to diminish the Reynolds shear stress mixing zones in the upper shear layer relative to the lower shear layer, which is more dramatic in the minor plane of the rectangular nozzle compared to the other configurations.

The influence of the nozzle geometry on the coherent structures in the interaction region was investigated using two-point spatial correlations and proper orthogonal decomposition (POD) analysis. For reference locations approaching the free surface, the two-point auto-correlation of the streamwise velocity fluctuations is growing, while that of the surface-normal velocity fluctuations is shrinking. This is consistent with the energy redistribution from surface-normal to the streamwise velocity fluctuations. The re-orientation of the rectangular nozzle to major axis increases the spatial coherence of the velocity fluctuations compared to the other nozzle configurations, indicating presence of more energetic eddies which might enhance the mixing at downstream. Unlike the other nozzle configurations, the two-point cross-correlation between the swirling strength and velocity fluctuations depicts a decorrelation for the rectangular jet with minor axis orientation with increasing distance from the surface, reflecting its faster deflection of the centerline, where the population density of

swirling strength is reduced. The POD results reveal that the fractional energy contribution of the most dominant mode is independent of nozzle geometry in the near field, but it is about 21% higher for the rectangular nozzle with major axis orientation than the other nozzles in the interaction regions. This leads to a faster convergence of cumulative energy in the interaction region of the major plane of the rectangular nozzle compared to the other nozzle configurations. These results are consistent with the two-point correlation measurements that show larger structure within the shear layers in the interaction region of the major plane of the rectangular jet.

Acknowledgements The authors gratefully acknowledge the support of this work by research grants from the Natural Sciences and Engineering Research Council of Canada.

Compliance with Ethical Standards

Conflict of Interest The authors declare that they have no conflict of interest.

References

1. Madnia, C.K., Bernal, L.P.: Interaction of a turbulent round jet with the free surface. *J. Fluid Mech.* **261**, 305–332 (1994)
2. Rahman, M.S., Tay, G.F.K., Essel, E.E., Tachie, M.F.: Effects of offset height on the turbulent characteristics of a surface attaching jet. *Int. J. Heat Fluid Flow.* **71**, 305–321 (2018)
3. Turan, C., Politano, M.S., Carrica, P.M., Weber, L.: Water entrainment due to spillway surface jets. *Int. J. Comput. Fluid D.* **21**(3–4), 137–153 (2007)
4. McQuirk, J.J., Rodi, W.: Mathematical modelling of three-dimensional heated surface jets. *J. Fluid Mech.* **95**(4), 609–633 (1979). <https://doi.org/10.1017/S0022112079001610>
5. Mi, J., Nathan, G.J.: Statistical properties of turbulent free jets issuing from nine differently-shaped nozzles. *Flow Turbul. Combust.* **84**, 583–606 (2010)
6. Aleyasin, S.S., Tachie, M.F., Koupriyanov, M.: Statistical properties of round, square, and elliptic jets at low and moderate Reynolds numbers. *J. Fluids Eng.* **139**(10), 101206 (2017). <https://doi.org/10.1115/1.4036824>
7. Aleyasin, S.S., Tachie, M.F., Koupriyanov, M.: PIV measurements in the near and intermediate field regions of jets issuing from eight different nozzle geometries. *Flow Turbul. Combust.* **99**, 329–351 (2017)
8. Tay, G.F.K., Rahman, M.S., Tachie, M.F.: Characteristics of a horizontal square jet interacting with the free surface. *Phys. Rev. Fluids.* **2**(6), 064607 (2017). <https://doi.org/10.1103/PhysRevFluids.2.064607>
9. Tay, G.F.K., Mishra, A., Kuhn, D.C.S., Tachie, M.F.: Free surface effects on the statistical properties of a submerged rectangular jet. *Phys. Fluids.* **29**, 025101 (2017). <https://doi.org/10.1063/1.4975155>
10. Anthony, D.G., Willmarth, W.W.: Turbulence measurement in a round jet beneath a free surface. *J. Fluid Mech.* **243**, 699–720 (1992)
11. Grinstein, F.F., Gutmark, E., Parr, T.: Near field dynamics of subsonic free square jets. A computational and experimental study. *Phys. Fluids.* **7**(6), 1483–1497 (1995). <https://doi.org/10.1063/1.868534>
12. Mi, J., Kalt, P., Nathan, G.J.: On turbulent jets issuing from notched-rectangular and circular orifice plates. *Flow Turbul. Combust.* **84**, 565–582 (2010)
13. Ho, C.M., Gutmark, E.: Vortex induction and mass entrainment in a small-aspect-ratio elliptic jet. *J. Fluid Mech.* **179**, 383–405 (1987)
14. Hussain, F., Husain, H.S.: Elliptic jets. Part 1. Characteristics of unexcited and excited jets. *J. Fluid Mech.* **208**, 257–320 (1989)
15. Gutmark, E., Grinstein, F.F.: Flow control with noncircular jets. *Annu. Rev. Fluid Mech.* **31**, 239–272 (1999)
16. Hammond, A.D.: Thrust Losses in Hovering for Jet Vtol Aircraft. Technical Report SP-116, NASA (1966)
17. Aleyasin, S.S., Fathi, N., Tachie, M.F., Vorobieff, P., Koupriyanov, M.: On the development of incompressible round and equilateral triangular jets due to Reynolds number variation. *J. Fluids Eng.* **140**(11), 111202 (2018). <https://doi.org/10.1115/1.4040031>

18. Wallker, D.T., Chen, C.-Y., Willmarth, W.W.: Turbulent structure in free-surface jet flows. *J. Fluid Mech.* **291**, 223–261 (1995)
19. Tian, J., Roussinova, V., Balachandar, R.: Characteristics of a jet in the vicinity of a free surface. *J. Fluids Eng.* **134**(1–12), 031204 (2012)
20. Sankar, G., Balachandar, R., Carriaveau, R.: Tailwater effects on the characteristics of a square jet near a free-surface. *J. Hydraul. Res.* **46**(4), 504–515 (2008)
21. Rajaratnam, N., Humphries, J.A.: Turbulent non-buoyant surface jets. *J. Hydraul. Res.* **22**(2), 103–115 (1984)
22. Ead, S.A., Rajaratnam, N.: Plane turbulent surface jets in shallow tailwater. *J. Fluid Eng.* **123**, 121–127 (2001)
23. Wen, Q., Kim, H.D., Liu, Y.Z., Kim, K.C.: Dynamic structures of a submerged jet interacting with a free surface. *Exp. Thermal Fluid Sci.* **57**, 396–406 (2014)
24. Wen, Q., Kim, H.D., Liu, Y.Z., Kim, K.C.: Structure analysis of a low Reynolds number turbulent submerged jet interacting with a free surface. *J. Fluids Eng.* **136**(1–16), 101104 (2014)
25. Rahman, M.S., Tachie, M.F.: Reynolds number effect on flow characteristics of surface single and twin jets. *J. Hydraul. Res.* 1–14 (2018). <https://doi.org/10.1080/00221686.2018.1522380>
26. Wang, X.K., Tan, S.K.: Experimental investigation of the interaction between a plane wall jet and a parallel offset jet. *Exp. Fluids.* **42**(4), 551–562 (2007)
27. Coleman, H.W., Steele, W.G.: Engineering application of experimental uncertainty analysis. *AIAA J.* **33**(10), 1888–1896 (1995)
28. Mi, J., Nathan, G.J., Nobes, D.S.: Mixing characteristics of axisymmetric free jets from a contoured nozzle, an orifice plate and a pipe. *J. Fluids Eng.* **123**(4), 878–883 (2001)
29. Quinn, W.R.: Experimental study of the near field and transition region of a free jet issuing from a sharp-edged elliptic orifice plate. *Eur. J. Mech. B. Fluids.* **26**, 583–614 (2007)
30. Ghasemi, A., Roussinova, V., Balachandar, R., Barron, R.M.: Reynolds number effects in the near-field of a turbulent square jet. *Exp. Thermal Fluid Sci.* **61**, 249–258 (2015)
31. Capone, A., Soldati, A., Romano, G.P.: Mixing and entrainment in the near field of turbulent round jets. *Exp. Fluids.* **54**(1434), (2013). <https://doi.org/10.1007/s00348-012-1434-x>
32. Grinstein, F.F., Devore, C.R.: Dynamics of coherent structures and transition to turbulence in free square jets. *Phys. Fluids.* **8**(5), 1237–1251 (1996). <https://doi.org/10.1063/1.868895>
33. Mullyadzhanov, R., Abdurakipov, S., Hanjalić, K.: Helical structures in the near field of a turbulent pipe jet. *Flow Turbul. Combust.* **98**(2), 367–388 (2017)
34. Westerweel, J., Fukushima, C., Pedersen, J.M., Hunt, J.C.R.: Mechanics of turbulent-non-turbulent interface of a jet. *Phys. Rev. Lett.* **95**(17), 174501 (2005). <https://doi.org/10.1103/PhysRevLett.95.174501>
35. Quinn, W.R.: Turbulent free jet flows issuing from sharp-edged rectangular slots: the influence of slot aspect ratio. *Exp. Thermal Fluid Sci.* **5**(2), 203–215 (1992)
36. Burattini, P., Antonia, R.A., Rajagopalan, S., Stephens, M.: Effect of initial conditions on the near-field development of a round jet. *Exp. Fluids.* **37**(1), 56–64 (2004)
37. Chen, N., Yu, H.: Mechanism of axis switching in low aspect-ratio rectangular jets. *Comput. Math. Appl.* **67**, 437–444 (2014)
38. Baddour, R.E., Zaghoul, A., Martinuzzi, R.: Entrainment properties of plane surface-jets in shallow current. *J. Hydraul. Eng.* **132**(4), 363–370 (2006)
39. Quinn, W.R., Militzer, J.: Experimental and numerical study of a turbulent free square jet. *Phys. Fluids.* **31**(5), 1017–1025 (1988)
40. Wgnanski, I., Fiedler, H.: Some measurements in the self-preserving jet. *J. Fluid Mech.* **38**, 577–612 (1969)
41. Xu, M., Zhang, J., Mi, J., Nathan, G.J., Kalt, P.A.M.: PIV measurements of turbulent jets issuing from triangular and circular orifice plates. *Sci. China Phys. Mech. Astron.* **56**(6), 1176–1186 (2013)
42. Ashcroft, G., Zhang, X.: Vortical structures over rectangular cavities at low speed. *Phys. Fluids.* **17**(1), 015104 (2005). <https://doi.org/10.1063/1.1833412>
43. Brown, G.L., Roshko, A.: On density effects and large structure in turbulent mixing layers. *J. Fluid Mech.* **64**, 775–816 (1974)
44. Essel, E.E., Nematollahi, A., Thacher, E.W., Tachie, M.F.: Effects of upstream roughness and Reynolds number on separated and reattached turbulent flow. *J. Turbul.* **16**(9), 872–899 (2015)
45. Nematollahi, A., Tachie, M.F.: Time-resolved PIV measurement of influence of upstream roughness on separated and reattached turbulent flows over a forward-facing step. *AIP Adv.* **8**(10), 105110 (2018). <https://doi.org/10.1063/1.5063455>
46. Essel, E.E., Tachie, M.F.: Roughness effects on turbulent flow downstream of a backward facing step. *Flow Turbul. Combust.* **94**, 125–153 (2015)

47. Gentile, V., Schrijer, F.F.J., Oudheusden, B.W.v., Scarano, F.: Afterbody effects on axisymmetric base flows. *AIAA J.* **54**(8), 2285–2294 (2016)
48. Ukeiley, L., Murray, N.: Velocity and surface pressure measurements in an open cavity. *Exp. Fluids.* **38**, 656–671 (2005)
49. Bian, S., Driscoll, J.F., Elbing, B.R., Ceccio, S.L.: Time resolved flow-field measurements of a turbulent mixing layer over a rectangular cavity. *Exp. Fluids.* **51**, 51–63 (2011)
50. Agelin-Chaab, M., Tachie, M.F.: Characteristics and structure of turbulent 3D offset jets. *Int. J. Heat Fluid Flow.* **32**(3), 608–620 (2011)
51. Volino, R.J., Schultz, M.P., Flack, K.A.: Turbulence structure in a boundary layer with two-dimensional roughness. *J. Fluid Mech.* **635**, 75–101 (2009)
52. Sirovich, L.: Turbulence and the dynamics of coherent structures, part 1: coherent structures. *Quart. J. Appl. Math.* **45**(3), 561–571 (1987)
53. Nyantekyi-Kwakye, B., Tachie, M.F., Clark, S., Malenchak, J., Muluye, G.: Experimental study of the flow structures of 3D turbulent offset jets. *J. Hydraul. Res.* **53**(6), 773–786 (2015)
54. Clark, S.P., Nyantekyi-Kwakye, B., Rahman, M.S., Boila, S., and Tachie, M.F.: Structure of 3D offset jets over a surface mounted square rib. 9th international symposium on turbulence and shear flow phenomena (TSFP-9), June 30–July 3, The University of Melbourne, Australia (2015)
55. Shinneeb, A.-M., Bugg, J.D., Balachandar, R.: Coherent structures in shallow water jets. *J. Fluids Eng.* **133**, 1–14 (2011)